

# Spin conductance of YIG thin films driven from thermal to subthermal magnons regime by large spin-orbit torque

N. Thierry,<sup>1</sup> A. Draveny,<sup>1</sup> V. V. Naletov,<sup>1,2</sup> L. Vila,<sup>1</sup> J.P. Attané,<sup>1</sup> C. Beigné,<sup>1</sup> G. de Loubens,<sup>3</sup> M. Viret,<sup>3</sup> N. Beaulieu,<sup>3,4</sup> J. Ben Youssef,<sup>4</sup> V. E. Demidov,<sup>5</sup> S. O. Demokritov,<sup>5,6</sup> A. Anane,<sup>7</sup> P. Bortolotti,<sup>7</sup> V. Cros,<sup>7</sup> and O. Klein<sup>1,\*</sup>

<sup>1</sup>*SPINTEC, CEA-Grenoble, CNRS and Université Grenoble Alpes, 38054 Grenoble, France*

<sup>2</sup>*Institute of Physics, Kazan Federal University, Kazan 420008, Russian Federation*

<sup>3</sup>*SPEC, CEA-Saclay, CNRS, Université Paris-Saclay, 91191 Gif-sur-Yvette, France*

<sup>4</sup>*LabSTICC, CNRS, Université de Bretagne Occidentale, 29238 Brest, France*

<sup>5</sup>*Department of Physics, University of Muenster, 48149 Muenster, Germany*

<sup>6</sup>*Institute of Metal Physics, Ural Division of RAS, Yekaterinburg 620041, Russian Federation*

<sup>7</sup>*Unité Mixte de Physique CNRS, Thales, Université Paris-Saclay, 91767 Palaiseau, France*

(Dated: December 3, 2024)

We report a study of the nonlinear regime of spin transport in a 18 nm thick extended thin film of Yttrium Iron Garnet (YIG). Propagating spin waves are generated and detected using direct and inverse spin Hall effects in two Pt wires deposited on top of the YIG film. The non-local resistance measured in the lateral devices clearly deviates from a linear behavior above an electrical current density in the Pt of about  $5 \cdot 10^{11} \text{ A/m}^2$ , where the spin transfer torque compensates the dissipation of long wavelength spin-wave modes. The data provides evidence for a gradual spectral shift from thermal to subthermal magnon transport as spin orbit torque is increased.

The recent demonstration that spin orbit effects in non-magnetic materials allow to create and detect pure spin currents [1–8] has triggered a renewed effort to develop a communication technology based solely on the spin degree of freedom. In this circumstance, magnetic materials are the natural spin conductors since they can efficiently propagate spin-waves or their quanta, magnons, which are the information carriers [9, 10]. Interestingly insulators are usually better spin conductors than metals and amongst them Yttrium Iron Garnet (YIG) is famous for having the lowest known damping parameter [11]. Recently the generation and detection of pure spin currents in YIG has been achieved by direct and inverse spin Hall effects in an adjacent metal with strong spin orbit interaction such as Pt [2, 12–19]. One fundamental issue is to determine the nature of the spin-wave modes excited by spin orbit torque (SOT). At the moment it seems that contradictory findings are reported by different experiments. On one hand, dynamical experiments monitoring the auto-oscillation regime in confined YIG geometries (micron-sized disks) have demonstrated that the magnetization dynamics is governed by coherent magnons, which have long wavelength and oscillate in the GHz range (subthermal magnons) [17, 18, 20]. On the other hand, non-local transport experiments monitoring the spatial decay of pure spin currents in YIG thin films have demonstrated that the dynamics is governed by thermal magnons [21], which have short wavelength and oscillate in the THz range [22–26]. At the heart of this debate lays the microscopic mechanism of spin transfer between a normal metal and a ferromagnet [27, 28]. The key parameter seems to be the level of instability created by the external flow of angular momentum [29], which depends on how the spin transfer torque com-

pensates the dissipative damping torque. There are already several other indications of the importance of this point. Recent experiments studying how a long wavelength mode, selectively excited by an external antenna, is amplified by SOT in a YIG|Pt waveguide and have shown the destructure of the coherent signal once the nonlinear threshold is reached [30]. Similar self-limiting effects have also been reported in the case of micron-sized YIG|Pt disks, while studying the auto-oscillation regime above criticality [18, 20]. These limitations reveal an intricate interplay between thermal and subthermal magnons [31, 32], which remains to be elucidated.

In this paper we propose to study in detail on how the nonlinear (NL) spin conduction regime emerges at room temperature in lateral device geometry, using YIG thin films subject to large SOT. A key here is to perform the experiment on high quality YIG films of small thickness. We shall use 18 nm thick YIG films grown by liquid phase epitaxy on a gadolinium gallium garnet substrate [15, 33]. Ferromagnetic resonance (FMR) spectroscopy of the bare film finds a damping parameter of  $\alpha_{\text{YIG}} = 4.4 \cdot 10^{-4}$  and an inhomogeneous broadening of about  $\Delta H_0 = 3.7 \text{ Oe}$ . The spontaneous magnetization  $4\pi M_s = 1.6 \text{ kG}$  as well as negligible magnetocrystalline anisotropy are inferred from FMR. On these films we have deposited Pt wires, 10 nm thick, 300 nm wide, and 20  $\mu\text{m}$  long. During the Pt deposition a reference YIG slab was covered under the same conditions for control purposes. On this reference slab, we measure an increase of the damping parameter by a factor roughly five to about  $\alpha_{\text{YIG|Pt}} = 2.4 \cdot 10^{-3}$ , which we attribute to a spin mixing conductance of the order of  $3 \cdot 10^{18} \text{ m}^{-2}$ . The electrical properties of the Pt layer are inferred from a reference wire patterned at one corner of the substrate and connected for 4-wire sensing.

TABLE I. Summary of the physical properties of the materials used in this study.

| YIG | $t_{\text{YIG}}$ (nm) | $4\pi M_s$ (G)                       | $\alpha_{\text{YIG}}$    | $\Delta H_0$ (Oe)                            |
|-----|-----------------------|--------------------------------------|--------------------------|--|
|     | 18                    | $1.6 \cdot 10^3$                     | $4.4 \cdot 10^{-4}$      | 3.7  |
| Pt  | $t_{\text{Pt}}$ (nm)  | $\rho$ ( $\mu\Omega\cdot\text{cm}$ ) | $\alpha_{\text{YIG Pt}}$ | $g_{\uparrow\downarrow}$ ( $\text{m}^{-2}$ ) |
|     | 10                    | 19.5                                 | $2.4 \cdot 10^{-3}$      | $3 \cdot 10^{18}$                            |

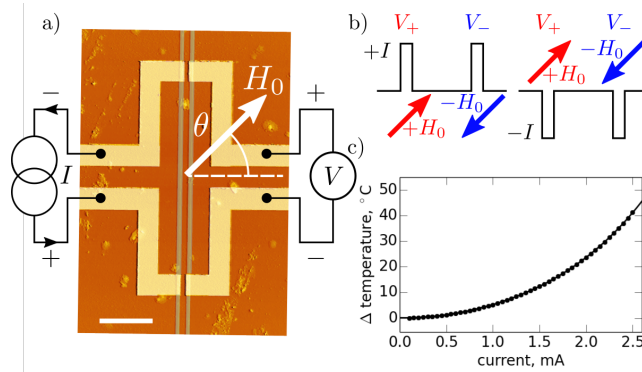


FIG. 1. (Color online) a) Atomic force microscopy image of the device. Two Pt wires (shown as vertical grey lines) are placed 1.2  $\mu\text{m}$  apart on top of a 18 nm thick YIG film (the scale bar is 5  $\mu\text{m}$  long). The non-local conductance I-V between the two wires is measured while an external magnetic field  $H_0$  is applied in-plane at a polar angle  $\theta$ . b) For each angle we perform four measurements ( $\pm H_0, \pm I$ ), using a pulse mode. Panel c) shows the temperature elevation produced in the Pt wire while increasing the current intensity.

The total resistance of the Pt at room temperature is  $R_0 = 1.3 \text{ k}\Omega$ , corresponding to a Pt resistivity of 19.5  $\mu\Omega\cdot\text{cm}$  [34]. All these numbers are summarized in Table 1. One should note that the obtained figures are close to the ones reported in our recent publication [18] despite the fact that both the YIG and Pt layers were elaborated by different techniques.

In lateral device geometry, one monitors the voltage along one wire as a current flows through a second wire. We shall first concentrate on the case of two wires separated by a gap of 1.2  $\mu\text{m}$ . FIG.1a shows the actual design. In this microscopy image, the Pt wires are the vertical lines colored in grey. The lateral device is placed between the poles of an electromagnet. It is mounted on a holder attached to a stepper motor which allows a polar rotation of the field. We define  $\theta$  as the angle made between the external magnetic field,  $H_0$ , and the perpendicular to the Pt wires. As shown in FIG.1a the Pt wires are connected by 50 nm thick Al electrodes colored in yellow. The choice of Al ensures that no SOT effect occurs outside the Pt wires. The two pairs of Al electrodes are connected on the left side to the current source and on the right side to the voltmeter. The current is injected in the device using 10 ms pulses inside a 10% duty cycle. The pulse method allows to limit heating of the

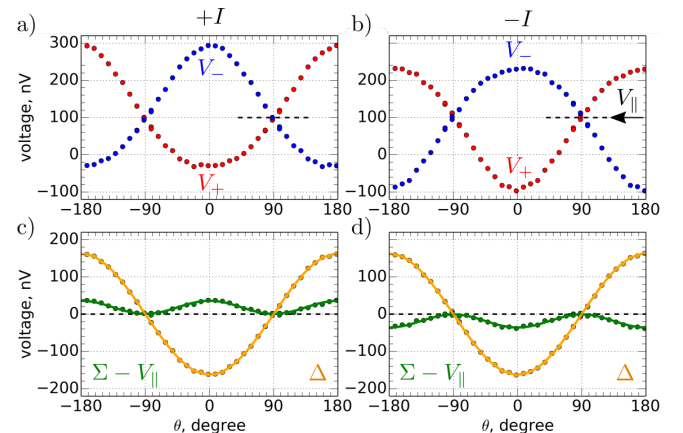


FIG. 2. (Color online) Polar angle,  $\theta$ , variation of the non-local voltages  $V_{\pm}$  measured respectively at bias magnetic field  $\mu_0 H_0 = \pm 2 \text{ kOe}$  using a) positive and b) negative current pulses of amplitude  $I = 1.5 \text{ mA}$ . We construct the voltage sum  $\Sigma = (V_+ + V_-)/2$  and the voltage difference  $\Delta = (V_+ - V_-)/2$  (respectively even/odd with respect to the  $H_0$ -polarity) whose angular dependences are shown in c) and d) for the two current polarities. The voltage sum is shown relative to the offset  $V_{\parallel}$ . The continuous lines are fits of the  $\Sigma$  and  $\Delta$  datasets by  $\cos \theta$  and  $\cos^2 \theta$  functions, respectively.

substrate, which thermalizes the lateral device. In our setup, the resistance  $R_I$  of the Pt wire is actually monitored during the pulse and used as a temperature sensor. In FIG.1c, we have plotted  $\kappa_{\text{Pt}}(R_I - R_0)/R_0$  as a function of the current  $I$ , where the coefficient  $\kappa_{\text{Pt}} = 254 \text{ K}$  is specific to Pt [35]. We see that the maximum temperature elevation of the wire is 42°C at the maximum current amplitude of 2.5 mA, corresponding to a current density of  $8 \cdot 10^{11} \text{ A/m}^2$ .

We now move on to the non-local transport measurement between the two Pt wires. At first, the amplitude of the applied field is set at  $\mu_0 H_0 = 2 \text{ kOe}$ , in order to avoid any influence of the Oersted field (which is about 50 Oe at the maximum current) and we also wish to use similar field bias as those in the study of the auto-oscillation regime in YIG|Pt disks [18]. For each polar angle  $\theta$ , we perform four measurements corresponding to all possible combinations of the polarities of the applied field and of the current ( $\pm H_0, \pm I$ ) as shown schematically in FIG.1b. FIG.2 shows the angular variation of the voltage produced on the right Pt wire when the current intensity is set at  $I = 1.5 \text{ mA}$  in the left wire. We have plotted in the same panel the voltages  $V_+$  and  $V_-$  obtained for opposite polarities of the applied magnetic field. We have separated in two different panels FIG.2a and FIG.2b the behaviors observed respectively for positive and negative current pulses. In the following the voltages will be defined relative to their offset  $V_{\parallel}$  measured at  $\theta = \pm 90^\circ$ , when the applied field is parallel to the wires. We believe that this offset [36] should be ascribed to thermoelectric effects produced by a small temperature difference at the

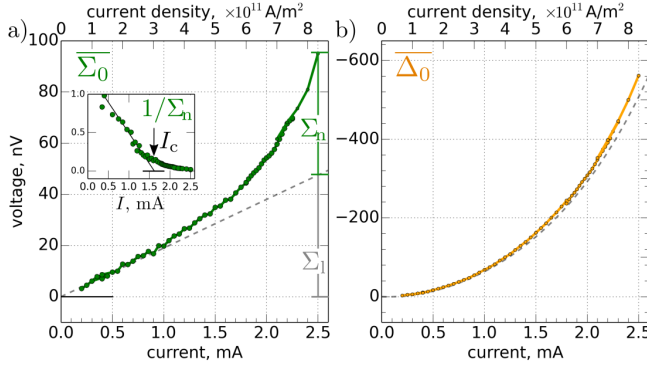


FIG. 3. (Color online) a) Current dependence of the polar variation of a) the  $\Sigma$  voltage and b) the  $\Delta$  voltage, averaged over positive and negative  $I$  contributions. a) The dashed line is a linear fit of the low current regime.  $\Sigma_n$  is the non-linear deviation from the extrapolated linear behavior  $\Sigma_l$ . The insert of a) shows the dependence of its inverse as a function of current. The dashed line in b) represents the scaled temperature variation in the Pt (cf FIG.1c).

two Pt|Al contacts of the detector circuit. Considering the Seebeck coefficient of Pt|Al [35], the offset measured at  $I = 1.5$  mA, corresponds to a temperature difference of less than  $0.03$  °C between the top and bottom contact electrodes, implying that the temperature is actually very homogeneous across the whole Pt wire.

A remarkable feature of FIG.2 is the asymmetry between  $V_+$  and  $V_-$ . This asymmetry inverts if the current polarity is inverted. To highlight this feature, we define the signal sum  $\Sigma = (V_+ + V_-)/2$  and the signal difference  $\Delta = (V_+ - V_-)/2$ , representing respectively the even and odd contributions with respect to the magnetic field polarity. Their angular dependence is plotted in FIG.2c for positive current pulses and in FIG.2d for negative current pulses. We find that the signal sum relative to the offset  $\Sigma_\theta = \Sigma - V_{\parallel}$  is odd in current, while the signal  $\Delta_\theta = \Delta$  is even in current. Thus the signal component even in  $H_0$  is also odd in  $I$ , and reciprocally. We have checked that this correspondence between the symmetries of  $\Sigma_\theta$  and of  $\Delta_\theta$  with respect to the polarities of  $H_0$  and  $I$  is always respected (within our measurement accuracy) for all the data presented below. In the linear regime, the symmetries of  $\Sigma_\theta$  and  $\Delta_\theta$  are the hallmark of respectively spin transfer effects (*i.e.*, the SOT) [18] and spin Seebeck effects (SSE) [37]. This attribution is supported by the observed angular dependences, which follows two completely different behaviors, one in  $\cos \theta$ , the other one in  $\cos^2 \theta$ , respectively, as previously shown [22]. The solid lines in FIG.2c and in FIG.2d are a fit by these two functions for each current polarity.

We now study how the signals attributed to SOT and SSE evolve when  $I$  is increased from 0.2 mA to 2.5 mA. For each value of  $I$ , we have recorded the full angular dependence and fitted the amplitudes of  $\Sigma_\theta = \Sigma_{0,I} \cos^2 \theta$

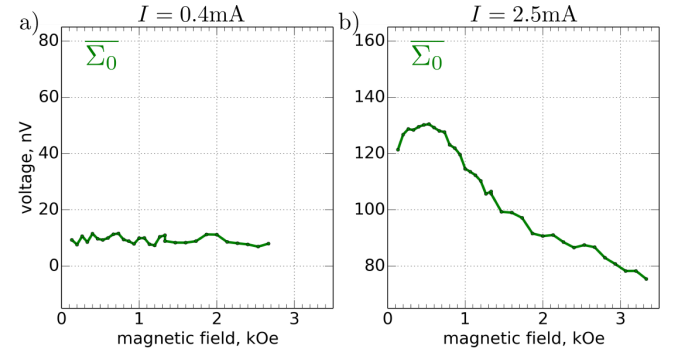


FIG. 4. (Color online) Variation of the sum voltage as a function of the applied magnetic field for two different current intensities below (a) and above (b) the critical current  $I_c$ .

and of  $\Delta_\theta = \Delta_{0,I} \cos \theta$ . From there, we have constructed the averaged contributions over the two current polarities  $\overline{\Sigma}_0 = (\Sigma_{0,+I} - \Sigma_{0,-I})/2$  and  $\overline{\Delta}_0 = (\Delta_{0,+I} + \Delta_{0,-I})/2$ .

FIG.3a shows the variation of  $\overline{\Sigma}_0$  as a function of  $I$ . At low current, the SOT signal follows first a linear behavior  $\Sigma_l$  which has already been shown to be dominated by thermal magnons [22]. Fitting a straight line through the  $I < 1$  mA data points, we find that the non-local resistance between the two Pt wires is  $\Sigma_l/I = 0.019$  mΩ. The striking novel feature observed in FIG.3a is the fact that the signal deviates from the linear behavior at large current intensity ( $I > 1$  mA). We define  $\Sigma_n$  as the deviation from the extrapolated linear behavior  $\Sigma_l$ . A fit of the inverse deviation [38, 39] vs.  $I$  provides an estimation of  $I_c \approx 1.6$  mA (see insert of FIG.3a), which corresponds to a current density  $J_c \approx 5 \cdot 10^{11} \text{ A/m}^2$ . We ascribe this density to the threshold current for damping compensation inside our YIG film. This value is very close to the threshold current observed at the same applied field ( $\mu_0 H_0 = 2$  kOe) in micron-sized disks with similar YIG|Pt characteristics [18]. In the latter case, the standing spin-wave mode excited in the GHz range was clearly identified as being a coherent motion of the magnetization. Since the dissipative torque is proportional to the frequency of the spin-wave mode, the fact that the NL threshold observed in FIG.3b is similar to the critical current density reported in ref.[18] suggests that the NL magnons excited above  $I_c$  are also long wavelength subthermal (more precisely subkelvin) magnons in the GHz range.

Quite remarkably, the enhancement  $\Sigma_n$  above  $I_c$  occurs very gradually. It is worth noticing that at the maximum charge current injected in our device,  $I = 2.5$  mA, (or  $I/I_c \approx 1.6$ ), we have only achieved  $\Sigma_n \approx \Sigma_l$ . Although this finding already provides a precious insight on how thermal magnons trickle into subthermal magnons as a function of the criticality parameter, a more quantitative analysis would require not only to take into account the interaction between these magnons' population but

also the normalization of the spectral sensitivity using a lateral device. Another issue that requires a careful treatment is the field asymmetry of the NL process. Indeed the creation of NL magnons by SOT only occurs for the field polarity that compensates the damping ( $\pm I \cdot V_{\pm} > 0$ ) and not the polarity that enhances the damping. Since  $\Sigma$  is the average of both contributions, the NL amount is only partially accounted in  $\Sigma_n$ . The difference should appear as an enhancement of the  $\Delta$ -signal. For symmetry reasons, this enhancement should be the same when  $I$  is inverted, and thus respects the fact that the  $\Delta$ -signal remains even in  $I$  on the whole current range. This deviation can be observed in FIG.3b, which shows the variation of  $\overline{\Delta}_0$  as a function of  $I$ . The observed behavior can be compared to the temperature elevation in the Pt measured in FIG.1c (shown here as a dashed line). The temperature elevation has been scaled by a coefficient  $\beta$  so that it matches the low current part of the curve ( $I < 1$  mA). The scaling applied is  $\beta = 13$  nV/K. We observe that the total  $\overline{\Delta}_0$  signal deviates from the dashed curve at large current amplitude. Further progress on this issue requires a better understanding of the different effects contributing to the  $\Delta$ -signal and the means to separate them.

Another insight about the nature of NL magnons can be obtained by studying the dependence of  $\overline{\Sigma}_0$  with the applied magnetic field [40]. The results are shown in FIG.4 for two values of the current  $I = 0.4$  and  $2.5$  mA, respectively below and above the NL threshold. While in the field range explored, the signal is almost independent of  $H_0$  when  $I$  is below  $I_c$ , it becomes strongly field dependent above  $I_c$ . This finding is consistent with a spectral shift of the nature of the propagating magnons between the two regimes. If indeed the dominant magnons are thermal magnons in the linear regime, their energy mostly depends on the exchange energy, which is much larger than the Zeeman energy. In contrast if subthermal magnons become dominant in the NL regime, because of their long wavelength, they are more sensitive to dipolar effects. Thus the sensitivity to the applied magnetic field amplitude observed in FIG.4b points toward the excitation of long wavelength magnons at large current, a conclusion that is consistent with the one inferred from the value of the threshold current. At constant current  $I$ , larger NL deviation voltage  $\Sigma_n$  with decreasing field observed in FIG.4b should be associated to an increase of surcriticality  $I/I_c$ , *i.e.* a decrease of  $I_c$  with field as expected from Kittel's law. This behavior reaches an extremum at low field due to the presence of inhomogeneous broadening [18].

We have repeated these studies on other lateral devices prepared either on a different YIG film (albeit with similar thickness and dynamical properties - as defined in Table 1) with different gaps between the 2 Pt wires. In all the lateral devices, the onset current density of the NL regime occurs at about the same value. FIG.5 shows

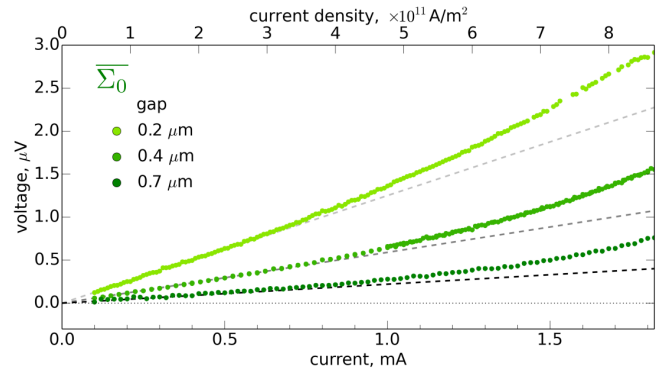


FIG. 5. (Color online) Variation of the  $\Sigma$  signal for different gaps between the two Pt wires.

the  $\Sigma$  voltage measured on 3 lateral devices with 3 different gaps respectively  $0.2$ ,  $0.4$ , and  $0.7$   $\mu$ m between the 2 wires. In addition to reducing the gap value compared to FIG.1, the Pt thickness is also reduced to 7 nm in order to enhance further the detected SOT signal. Comparing the value of  $\Sigma_l$  between the different gaps, one can observe that it decays with increasing separation. The behavior follows a characteristic decay length of about  $0.4$   $\mu$ m (a value confirmed by independent microfocus Brillouin light scattering studies performed on the same batch). The important feature of FIG.5 is that the ratio  $\Sigma_n/\Sigma_l$  measured above  $J_c$  increases with decreasing  $\Sigma_l$  suggesting that the characteristic propagation length of the NL magnons is greater than the characteristic propagation length of thermal magnons: a behavior again consistent with ascribing a spectral shift towards the low energy part of the spectrum.

In summary, we have measured the spin transport of YIG|Pt lateral devices in the NL regime. Deviation from a linear regime is observed when the threshold for the spin transfer torque to compensate the dissipation of long wavelength spin-wave modes is reached. The non-local resistance observed in the lateral devices is interpreted as a gradual spectral shift from a transport predominantly mediated by thermal magnons to a transport predominantly mediated by subthermal magnons as the current is increased. Further analysis of this spectral shift should provide insight information about the microscopic mechanism of SOT and mode competition that exists in magnetic films.

This research was supported in part by the CEA program NanoScience (project MAFETY), by the priority program SPP1538 Spin Caloric Transport (SpinCaT) of the DFG and by the program Megagrant 14.Z50.31.0025 of the Russian ministry of Education and Science. VVN acknowledges fellowship from the emergence strategic program of UGA, and Russian program of competitive growth of KFU. We thank G. Zhand, T. van Pham, A. Brenac for their help in the fabrication of the lateral devices.

\* Corresponding author: oklein@cea.fr

[1] S. O. Valenzuela and M. Tinkham, *Nature* **442**, 176 (2006).

[2] Y. Kajiwara, K. Harii, S. Takahashi, J. Ohe, K. Uchida, M. Mizuguchi, H. Umezawa, H. Kawai, K. Ando, K. Takanashi, S. Maekawa, and E. Saitoh, *Nature* **464**, 262 (2010).

[3] I. M. Miron, K. Garello, G. Gaudin, P.-J. Zermatten, M. V. Costache, S. Auffret, S. Bandiera, B. Rodmacq, A. Schuhl, and P. Gambardella, *Nature* **476**, 189 (2011).

[4] J.-C. Rojas-Sánchez, L. Vila, G. Desfonds, S. Gambarelli, J. P. Attan, J. M. D. Teresa, C. Magn, and A. Fert, *Nature Comm.* **4**, 2944 (2013).

[5] S. Sangiao, J. M. De Teresa, L. Morellon, I. Lucas, M. C. Martínez-Velarrete, and M. Viret, *Appl. Phys. Lett.* **106**, 172403 (2015).

[6] A. R. Mellnik, J. S. Lee, A. Richardella, J. L. Grab, P. J. Mintun, M. H. Fischer, A. Vaezi, A. Manchon, E.-A. Kim, N. Samarth, and D. C. Ralph, *Nature* **511**, 449 (2014).

[7] E. Lesne, Y. Fu, S. Oyarzun, J. C. Rojas-Sánchez, D. C. Vaz, H. Naganuma, G. Sicoli, J.-P. Attan, M. Jamet, E. Jacquet, J.-M. George, A. Barthlmy, H. Jaffrs, A. Fert, M. Bibes, and L. Vila, *Nature Mater.* **15**, 1261 (2016).

[8] J.-Y. Chauleau, M. Boselli, S. Gariglio, R. Weil, G. de Loubens, J.-M. Triscone, and M. Viret, *EPL* **116**, 17006 (2016).

[9] V. V. Kruglyak, S. O. Demokritov, and D. Grundler, *J. Phys. D* **43**, 264001 (2010).

[10] A. V. Chumak, V. I. Vasyuchka, A. A. Serga, and B. Hillebrands, *Nature Phys.* **11**, 453 (2015).

[11] E. G. Spencer, R. C. LeCraw, and A. M. Clogston, *Phys. Rev. Lett.* **3**, 32 (1959).

[12] Z. Wang, Y. Sun, M. Wu, V. Tiberkevich, and A. Slavin, *Phys. Rev. Lett.* **107**, 146602 (2011).

[13] E. Padrón-Hernández, A. Azevedo, and S. M. Rezende, *Appl. Phys. Lett.* **99**, 192511 (2011).

[14] A. V. Chumak, A. A. Serga, M. B. Jungfleisch, R. Neb, D. A. Bozhko, V. S. Tiberkevich, and B. Hillebrands, *Appl. Phys. Lett.* **100**, 082405 (2012).

[15] C. Hahn, G. de Loubens, O. Klein, M. Viret, V. V. Naletov, and J. Ben Youssef, *Phys. Rev. B* **87**, 174417 (2013).

[16] O. d'Allivy Kelly, A. Anane, R. Bernard, J. Ben Youssef, C. Hahn, A. H. Molpeceres, C. Carretero, E. Jacquet, C. Deranlot, P. Bortolotti, R. Lebourgeois, J.-C. Mage, G. de Loubens, O. Klein, V. Cros, and A. Fert, *Appl. Phys. Lett.* **103**, 082408 (2013).

[17] A. Hamadeh, O. d'Allivy Kelly, C. Hahn, H. Meley, R. Bernard, A. H. Molpeceres, V. V. Naletov, M. Viret, A. Anane, V. Cros, S. O. Demokritov, J. L. Prieto, M. Muñoz, G. de Loubens, and O. Klein, *Phys. Rev. Lett.* **113**, 197203 (2014).

[18] M. Collet, X. de Milly, O. d'Allivy Kelly, V. Naletov, R. Bernard, P. Bortolotti, J. Ben Youssef, V. Demidov, S. Demokritov, J. Prieto, M. Muñoz, V. Cros, A. Anane, G. de Loubens, and O. Klein, *Nature Commun.* **7**, 10377 (2016).

[19] V. Lauer, D. A. Bozhko, T. Brcher, P. Pirro, V. I. Vasyuchka, A. A. Serga, M. B. Jungfleisch, M. Agrawal, Y. V. Kobljanskyj, G. A. Melkov, C. Dubs, B. Hillebrands, and A. V. Chumak, *Appl. Phys. Lett.* **108**, 012402 (2016).

[20] V. E. Demidov, M. Evelt, V. Bessonov, S. O. Demokritov, J. L. Prieto, M. Muoz, J. Ben Youssef, V. V. Naletov, G. de Loubens, O. Klein, M. Collet, P. Bortolotti, V. Cros, and A. Anane, *Sci. Rep.* **6**, 32781 (2016).

[21] Thermal magnons:  $hf \approx k_B T$ ; subthermal magnons  $hf \approx \gamma H_0$ .

[22] L. J. Cornelissen, J. Liu, R. A. Duine, J. Ben Youssef, and B. J. van Wees, *Nature Phys.* **11**, 1022 (2015).

[23] S. T. B. Goennenwein, R. Schlitz, M. Pernpeintner, K. Ganzhorn, M. Althammer, R. Gross, and H. Huebl, *Appl. Phys. Lett.* **107**, 172405 (2015).

[24] J. Li, Y. Xu, M. Aldosary, C. Tang, Z. Lin, S. Zhang, R. Lake, and J. Shi, *Nature Commun.* **7**, 10858 (2016).

[25] H. Wu, C. H. Wan, X. Zhang, Z. H. Yuan, Q. T. Zhang, J. Y. Qin, H. X. Wei, X. F. Han, and S. Zhang, *Phys. Rev. B* **93**, 060403 (2016).

[26] L. J. Cornelissen, K. J. H. Peters, G. E. W. Bauer, R. A. Duine, and B. J. van Wees, *Phys. Rev. B* **94**, 014412 (2016).

[27] J. Slonczewski, *J. Magn. Magn. Mater.* **159**, L1 (1996).

[28] L. Berger, *Phys. Rev. B* **54**, 9353 (1996).

[29] V. E. Demidov, S. Urazhdin, E. R. J. Edwards, M. D. Stiles, R. D. McMichael, and S. O. Demokritov, *Phys. Rev. Lett.* **107**, 107204 (2011).

[30] M. Evelt, V. E. Demidov, V. Bessonov, S. O. Demokritov, J. L. Prieto, M. Muoz, J. Ben Youssef, V. V. Naletov, G. de Loubens, O. Klein, M. Collet, K. Garcia-Hernandez, P. Bortolotti, V. Cros, and A. Anane, *Appl. Phys. Lett.* **108**, 172406 (2016).

[31] B. Flebus, P. Upadhyaya, R. A. Duine, and Y. Tserkovnyak, *Phys. Rev. B* **94**, 214428 (2016).

[32] S. A. Bender and Y. Tserkovnyak, *Phys. Rev. B* **93**, 064418 (2016).

[33] V. Castel, N. Vlietstra, B. J. van Wees, and J. Ben Youssef, *Phys. Rev. B* **86**, 134419 (2012).

[34] The Pt wire resistance increases by 0.028% when  $\theta$  is rotated between 0 and 90°. This figure represents the spin Hall magnetoresistance of the Pt on YIG [15] and is consistent with the spin mixing conductance inferred from the FMR and the spin transport parameters of the Pt [41].

[35] H. Landolt and R. Börnstein, *Group III, Condensed Matter*, Numerical data and functional relationship in Science and technology (Springer, Berlin, 1970).

[36] In this current range,  $V_{\parallel}$  is independent of the current polarity and it scales with the temperature of Pt.

[37] K. Uchida, J. Xiao, H. Adachi, J. Ohe, S. Takahashi, J. Ieda, T. Ota, Y. Kajiwara, H. Umezawa, H. Kawai, G. E. W. Bauer, S. Maekawa, and E. Saitoh, *Nature Mater.* **9**, 894 (2010).

[38] A. Slavin and V. Tiberkevich, *IEEE Trans. Magn.* **45**, 1875 (2009).

[39] A. Hamadeh, G. de Loubens, V. V. Naletov, J. Grollier, C. Ulysse, V. Cros, and O. Klein, *Phys. Rev. B* **85**, 140408 (2012).

[40] L. J. Cornelissen and B. J. van Wees, *Phys. Rev. B* **93**, 020403 (2016).

[41] Y.-T. Chen, S. Takahashi, H. Nakayama, M. Althammer, S. T. B. Goennenwein, E. Saitoh, and G. E. W. Bauer, *Phys. Rev. B* **87**, 144411 (2013).